The first order statistics of backscatter from the fractal branching vasculature

Kevin J. Parker[a)]

Department of Electrical and Computer Engineering, University of Rochester, Rochester, New York 14627, USA

The issue of speckle statistics from ultrasound images of soft tissues such as the liver has a long and rich history. A number of theoretical distributions, some related to random scatterers or fades in optics and radar, have been formulated for pulse-echo interference patterns. This work proposes an alternative framework in which the dominant echoes are presumed to result from Born scattering from fluid-filled vessels that permeate the tissue parenchyma. These are modeled as a branching, fractal, self-similar, multiscale collection of cylindrical scatterers governed by a power law distribution relating to the number of branches at each radius. A deterministic accounting of the echo envelopes across the scales from small to large is undertaken, leading to a closed form theoretical formula for the histogram of the envelope of the echoes. The normalized histogram is found to be related to the classical Burr distribution, with the key power law parameter directly related to that of the number density of vessels vs diameter, frequently reported in the range of 2 to 4. Examples are given from liver scans to demonstrate the applicability of the theory.
© 2019 Acoustical Society of America. https://doi.org/10.1121/1.5132934

[JFL]

I. INTRODUCTION

A century of research on scattering of light and sound has accumulated since the landmark papers of Rayleigh (1897, 1918a) and today, every day, an uncountable number of ultrasound scans are created from tissue backscatter. In normal soft tissues such as the liver, prostate, and thyroid, the source of the backscatter is presumed to be internal inhomogeneities which have been typically modeled as statistical inhomogeneities or spherical shapes linked to the cellular structures of the soft tissue.

For example, Chivers (1977) considered both exponential and Gaussian correlation models in his survey of tissue scattering. Waag and colleagues (Waag et al., 1982; Campbell and Waag, 1984b; Waag et al., 1989a, 1989b) considered Gaussian and modified Gaussian correlation models. Lizzi et al. (1983) established a framework for analysis of scattered ultrasound from tissues, including a model of very small scattering sites that were Poisson-distributed in space, and then later including spherical shapes that have been incorporated into quantitative ultrasound studies (Mamou and Oelze, 2013). Insana and colleagues (1990) considered three correlation functions for random media, related to fluid spheres, spherical shells, and a Gaussian behavior. These were applied to a number of phantoms and tissues (Insana and Brown, 1993). Shung and Thieme (1993) demonstrated the scattering of red blood cells which in a dispersed form exhibit classical Rayleigh scattering behavior at the frequencies commonly used in ultrasound scans of adult humans. The importance of clustering of red blood cells was analyzed by Fontaine et al. (2002) and Savery and Cloutier (2001, 2005).

A recently proposed alternative hypothesis is that within soft and macroscopically isotropic tissues such as the liver, the dominant parenchymal cellular structure forms the *reference media* and the fractal branching vasculature and fluid channels form the *weak scattering structures* within the Born approximation. The consequences of this new framework are significant, as the canonical structural shape must be cylindrical, not spherical, and the self-similar or fractal or multiscale nature of the branching fluid channels must be considered within the ensemble average.

The second order statistics, specifically the ensemble-averaged backscatter, has been recently considered for this new hypothesis (Parker, 2019; Parker et al., 2019), and the fractal branching cylindrical models were found to predict a power law (f^γ) increase in backscatter vs frequency for tissues such as the liver, matching the experimental results from the early leading studies (Campbell and Waag, 1984a; Zagzebski et al., 1993).

However, the first order statistics of soft tissues under the new hypothesis have not yet been resolved. The distribution of the envelope of echoes from the liver and other soft tissues has been an intense subject of research over the years (Burckhardt, 1978; Bamber and Dickinson, 1980; Sleefe and Lele, 1988; Landini and Verrazzani, 1990; Wear et al., 1997; Cramblitt and Parker, 1999; Kutay et al., 2001, 2003; Laporte et al., 2009). Based on models originating from radar and optical speckle, and on one-dimensional convolution models, the envelope of radio frequency (RF) echoes have been fit to Rayleigh, Gamma, Rician, Homodyne-K, and other distributions. It was hoped that some measure of tissue structure, such as the number of discrete scatterers per unit volume, could be estimated from these distribution functions; however, no definitive consensus has been achieved.

[a)]Electronic mail: kevin.parker@rochester.edu

With the goal of clarifying the dominant mechanisms at work in pulse-echo imaging, we depart from earlier frameworks in two significant ways: first, the scattering structures are assumed to be a multiscale set of cylindrical vessels of radius a with a density distribution that follows a power law, $N(a) = N_0/a^b$. Second, we derive a fully deterministic (not probabilistic) ensemble of echo amplitudes based on the dominant (maximum) signals obtained from the three-dimensional (3D) convolution of a pulse with the isotropic ensemble of scattering cylindrical vessels. The result is a model of the envelope histogram that is deterministic and somewhat resembles—but is not equal to—the Rayleigh distribution. In this framework a key tissue parameter of the envelope distribution is the power law parameter b, which captures the multiscale distribution of vessels from the few large vessels to the greater numbers of smaller vessels.

II. THEORY

Assume a broadband pulse propagating in the x direction is given by separable functions,

$$P\left(y, z, t - \frac{x}{c}\right) = G_y(y, \sigma_y) G_z(z, \sigma_z) P_x\left(t - \frac{x}{c}\right), \qquad (1)$$

where $G_y(y, \sigma_y) = \exp\left[-y^2/2\sigma_y^2\right]$, i.e., Gaussian in the y and z directions, and where the pulse shape P_x in the x direction is given by

$$P_x(x) = GH_2\left(\frac{x}{\sigma_x}\right)\exp\left(-\frac{x}{\sigma_x}\right)^2 = \mathbf{e}^{-x^2/\sigma_x^2}\left(\frac{4x^2}{\sigma_x^2} - 2\right), \qquad (2)$$

where GH_2 is a second-order Hermite polynomial for the pulse shape with a spatial scale factor of σ_x (Poularikas, 2010; Parker, 2016), representing a broadband pulse. Its spatial Fourier transform is then

$$\begin{aligned}{}^{3D}\Im\{P(x, y, z, t = 0)\} \\ = \left(4\mathbf{e}^{-k_x^2\pi^2\sigma_x^2}k_x^2\pi^{5/2}\sigma_x^3\right)\left(\mathbf{e}^{-2k_y^2\pi^2\sigma_y^2}\sqrt{2\pi}\sigma_y\right) \\ \times \left(\mathbf{e}^{-2k_z^2\pi^2\sigma_z^2}\sqrt{2\pi}\sigma_z\right),\end{aligned} \qquad (3)$$

where we use Bracewell's (1965b) convention for the form of the Fourier transform.

Using a 3D convolution model (Bamber and Dickinson, 1980; Macovski, 1983; Prince and Links, 2015), we will determine the *dominant* echoes from the pulse interacting with each generation of elements in a branching, fractal, self-similar set of vessels shown in Fig. 1, and whose number density follows a power law behavior $N(a) = N_0/a^b$. From these echoes, the histogram of envelopes is determined by summing up over all the fractal branches.

Assuming an isotropic spatial and angular distribution of each generation of fractal branching structures, we need to consider a basic element across all angles of incidence with respect to the propagating wave and across all size scales, from very small microchannels of fluid to the largest arteries and veins that can exist within the organ. Specifically, we will examine a long fluid-filled cylinder of radius a,

$$f(r) = \begin{cases} \kappa_0 & r \leq a \\ 0 & r > a \end{cases}$$

$$F(\rho) = \frac{\kappa_0 \cdot a \cdot J_1[2\pi a \cdot \rho]}{\rho}, \qquad (4)$$

where κ_0 is the fractional variation in compressibility, assumed to be $\ll 1$ consistent with the Born formulation, $F(\rho)$ represents the Hankel transform, which is the two-dimensional Fourier transform of a radially symmetric function, $J_1[\cdot]$ is a Bessel function of order 1, and ρ is the spatial frequency. The fractional variation in compressibility, κ_0, between blood vessels and liver parenchyma has been estimated to be approximately 0.03, or a 3% difference based on published data (Parker, 2019).

Consider first one infinitely long cylinder with material property $f(r)$—symmetric—as shown in Fig. 2(a) and tilted at some arbitrary angle in a spherical coordinate system. It has a 3D Fourier transform that is a thin disk, shown in Fig. 2(b) (delta function k_z but shown with finite thickness to make the graphic easier to draw and visualize). A particular radius of spatial frequency equal to q_0 is shown for reference. The shape of the 3D spatial Fourier transform of the pulse is shown in Fig. 2(c).
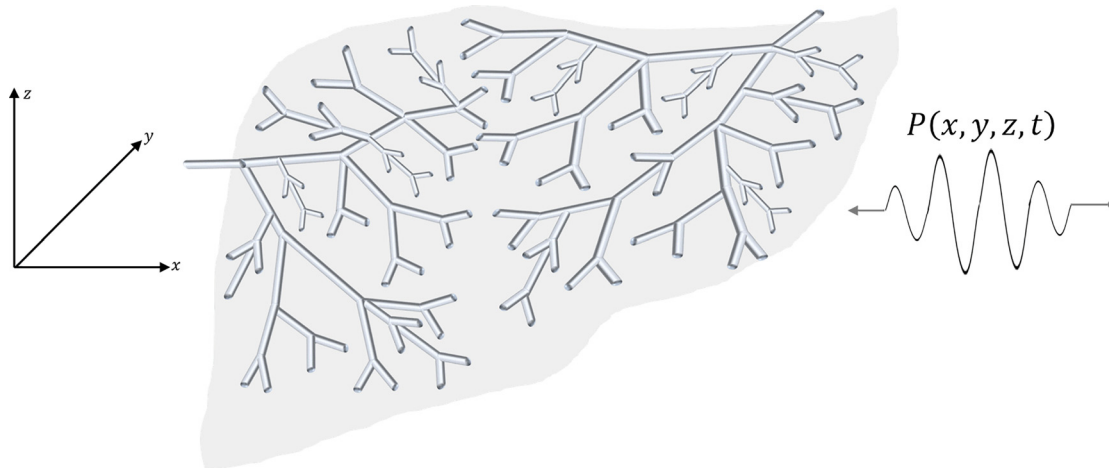

FIG. 1. (Color online) Model of 3D convolution of a pulse with the fractal branching cylindrical fluid-filled channels in a soft tissue.
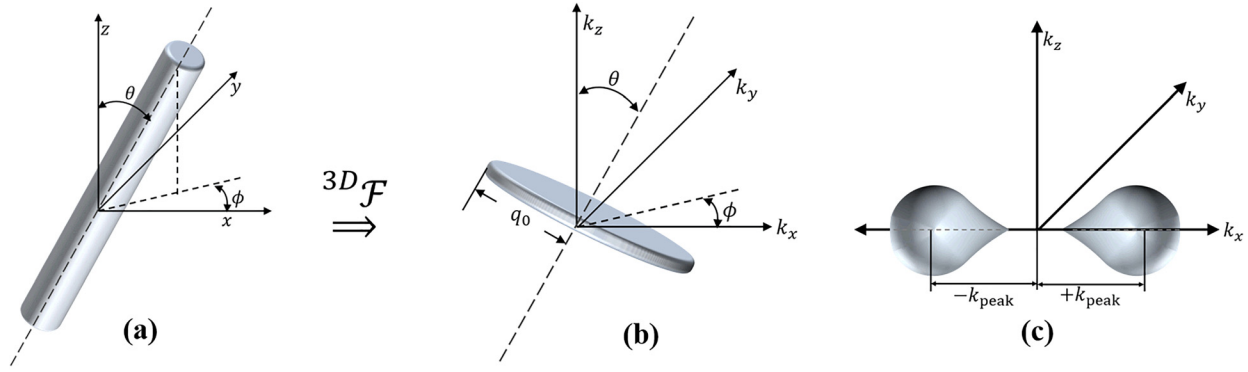
FIG. 2. (Color online) A cylindrical function (a) and its Hankel transform represented in 3D Fourier transform space (b). Rotations around spherical coordinates similarly rotate the corresponding transform. The transform of a propagating pulse is shown in (c). The maximum product of (b) and (c) arrives when the angle θ approaches zero.

One can see from Fig. 2 that the convolution of the pulse with a cylinder of radius a is dominated by the case where the cylinder is perpendicular to the direction of the forward propagating pulse, the x axis in our case. For all other orientations, the delta function of the cylindrical transform shown in Fig. 2(b) is misaligned with respect to the transform of the pulse shown in Fig. 2(c). Thus, assuming an optimal alignment, the 3D convolution result is given by the product of the transforms,

$$
\begin{aligned}
&{}^{3D}\Im\{\text{echo}(x,y,z,t=0)\} \\
&= \Im^{3D}\{p(x,y,z)\} \cdot (k_x)^2 \Im^{3D}\{\text{cylinder}(x,y,z)\} \\
&= \left(\left(4e^{-k_x^2\pi^2\sigma_x^2}k_x^2\pi^{5/2}\sigma_x^3\right)\left(e^{-2k_y^2\pi^2\sigma_y^2}\sqrt{2\pi}\sigma_y\right) \right. \\
&\quad \times \left(e^{-2k_z^2\pi^2\sigma_z^2}\sqrt{2\pi}\sigma_z\right)\right) \cdot (k_x)^2 \kappa_0\left(a\left[\frac{1}{\sqrt{k_x^2+k_y^2}}\right]\right. \\
&\quad \left.\left. \cdot\left(J_1\left[2a\pi\sqrt{k_x^2+k_y^2}\right]\right)\right)\delta[k_z],
\end{aligned}
\tag{5}
$$

where $t=0$ is assigned to the central peak of the echo, and the $(k_x)^2$ term pre-multiplying the cylinder transform stems from the Laplacian spatial derivative in the Born scattering formulation (Rayleigh, 1918a; Morse and Ingard, 1987) and in the 3D convolution model (Gore and Leeman, 1977; Bamber and Dickinson, 1980).

By Parseval's theorem, the integral of the square of the transform equals the integral of the square of the echo, and after integration over the delta function in k_z,

$$
\begin{aligned}
&\int (\text{echo}(t))^2 dt \\
&= \sigma_z^2\kappa_0^2 \int_{kx=-\infty}^{\infty}\int_{ky=-\infty}^{\infty}\left(8e^{-\pi^2\left(k_x^2\sigma_x^2+2k_y^2\sigma_y^2\right)}k_x^2\pi^{7/2}\sigma_x^3\sigma_y\right)^2 \\
&\quad \cdot (k_x^2)^2\left(a\left[\frac{1}{\sqrt{k_x^2+k_y^2}}\right]\cdot\left(J_1\left[2a\pi\sqrt{k_x^2+k_y^2}\right]\right)\right)^2 \\
&\quad \cdot dk_x dk_y.
\end{aligned}
\tag{6}
$$

The square root of this gives the root-mean-square (RMS) amplitude of the echo, as a function of the radius a, shown for the practical span of $0 < a/\sigma_x < 10$ in Fig. 3. We will associate the RMS amplitude from each echo with a proportionally higher maximum value of the envelope, as a function of cylinder radius a. This single value mapping is justified in the Appendix.

Also shown in Fig. 3 is an approximation which will be useful for deriving a closed form solution, the approximation is of the form $A[a] = A_0\sqrt{a-a_{\min}}$, justified by the nearly linear increase in the energy term above some minimum threshold, and the asymptotic modulus of $J_1(ak)$ which is proportional to $\sqrt{2/(\pi ak)}$ (Abramowitz and Stegun, 1964) as ak becomes large. Of course the exact shape is dependent on the particular pulse shape's spectrum, for example, if instead of a GH_2 we use a $k_x \cdot \text{sech}[k_x]$ bandpass for $\Im\{P_x(x)\}$, which has an exponential asymptotic tail instead of a Gaussian, then the result is shown in Fig. 4. So as a general approximation, we apply the relation $A[a] = A_0\sqrt{a-a_{\min}}$ for $a > a_{\min}$. The parameter $a_{\min}$ depends on a number of factors, including the dynamic range selected (for example, 45 dB) and the Rayleigh scattering (long wavelength, small a) behavior of the cylinder interacting with the particular pulse transmit signal, along with the noise floor and quantization floor of the receiver.
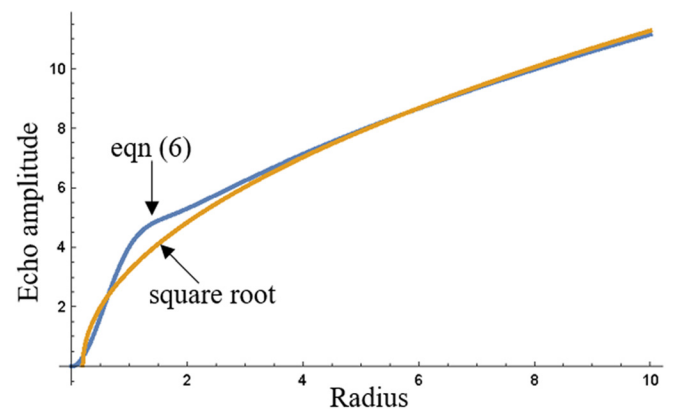

FIG. 3. (Color online) The RMS echo amplitude (vertical axis, arbitrary units) vs cylinder radius normalized by σ_x from Eq. (6), and square root approximation, assuming a GH_2 pulse.
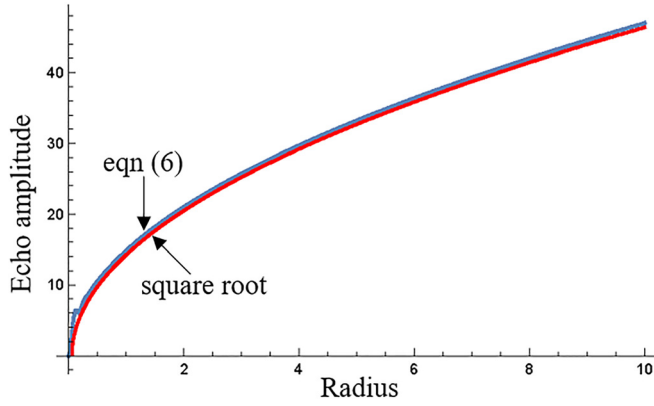
Kevin J. Parker

FIG. 4. (Color online) The RMS echo amplitude for a second bandpass pulse shape with exponential tails vs normalized radius of a scattering cylinder, and a square root approximation.

Now, applying the general theory of transformed distributions (see the Appendix), we have within the ensemble the number density of vessels at different radii given by $N[a] = N_0/a^b$, and this will be transformed into the distribution of amplitudes, $A(a)$. The general rule is

$$N[A] = \frac{1}{dA/da} N[a]. \tag{7}$$

In our case, the derivative $dA/da = [(1/2)A_0]/\sqrt{a - a_{min}}$, and the inverse function is $a[A] = (A/A_0)^2 + a_{min}$. Thus, substituting these into Eq. (7) the distribution $N[A]$ is

$$N[A] = \frac{2N_0 A}{A_0^2 \left[(A/A_0)^2 + a_{min} \right]^b}. \tag{8}$$

So, for example, if $b = 2$ and A_0 and N_0 are unity, then $N[A] = 2A/(A^2 + a_{min})^2$, and this is plotted in Fig. 5 along with variations in parameters. This provides a four-parameter fit $\{N_0, A_0, a_{min}, b\}$ to a histogram taken from a reasonably sized region of interest (ROI) within a vascularized tissue or organ, assuming an isotropic and spatially uniform distribution across the ROI.

However, of these four parameters, N_0, A_0, and a_{min} are influenced by system parameters such as amplifier gain and the size of the ROI. To simplify the analysis, one can

normalize by the integral of the distribution $\int N[A] dA = N_0/ [(b - 1)(a_{min})^{b-1}]$ to form a proper probability density function (PDF), which integrates to unity

$$N_n[A] = \frac{2A(a_{min})^{b-1}(b - 1)}{A_0^2 \left[\left(\frac{A}{A_0} \right)^2 + a_{min} \right]^b}. \tag{9}$$

Furthermore, by substituting $\lambda = A_0 \sqrt{a_{min}}$, we find this reduces to a two-parameter distribution

$$N_n[A] = \frac{2A(b - 1)}{\lambda^2 \left[\left(\frac{A}{\lambda} \right)^2 + 1 \right]^b}, \tag{10}$$

which is a Burr type XII distribution with $c = 2$ (Burr, 1942; Rodriguez, 1977). Thus, the normalized distribution offers a simplification to a two-parameter distribution with analytic expressions for PDF, cumulative distribution function (CDF), and moments (Rodriguez, 1977).

Using the notations from Bracewell (1965a), we calculate by integration the centroid of the distribution and find the expected value of the normalized histogram

$$\langle A \rangle = \frac{\lambda(-1 + b)\sqrt{\pi}\Gamma\left[-\frac{3}{2} + b \right]}{2\Gamma[b]} \quad \text{for } b > \frac{3}{2}, \tag{11}$$

where $\Gamma[\cdot]$ is the gamma function (Abramowitz and Stegun, 1964). Similarly, the mean square abscissa can found by integration

$$\langle A^2 \rangle = \frac{\lambda^2}{b - 2} \quad \text{for} \quad b > 2. \tag{12}$$

In a similar way, the variance can be calculated, and then a measure of signal-to-noise ratio (SNR) defined by the mean value over the standard deviation is

$$\text{SNR} = \frac{\langle A \rangle}{\sigma_A} = \frac{\Gamma\left[-\frac{3}{2} + b \right]}{\sqrt{4(b - 2)\Gamma(b - 2)^2/\pi - \Gamma\left(-\frac{3}{2} + b \right)}}. \tag{13}$$
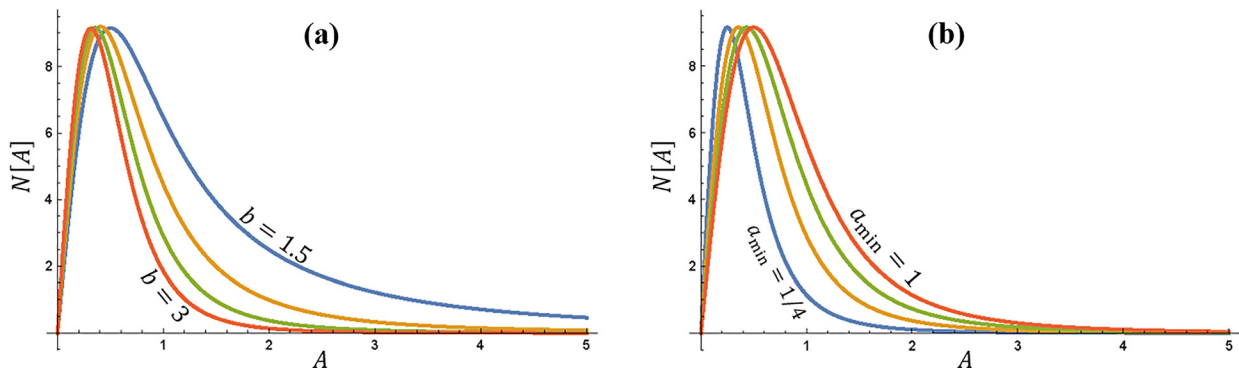

FIG. 5. (Color online) The proposed histogram function of envelope amplitudes A, having the form $A/(A^2 + a_{min})^b$. In (a) are normalized functions where $a_{min} = 1/2$ and the power law parameter b is 3, 2.5, 2, and 1.5. In (b) are normalized functions where the power law parameter is fixed at 2.5; however, a_{min} is varied as 1/4, 1/2, 3/4, and 1. Vertical axis: counts (arbitrary units); horizontal axis: envelope amplitude (arbitrary units).
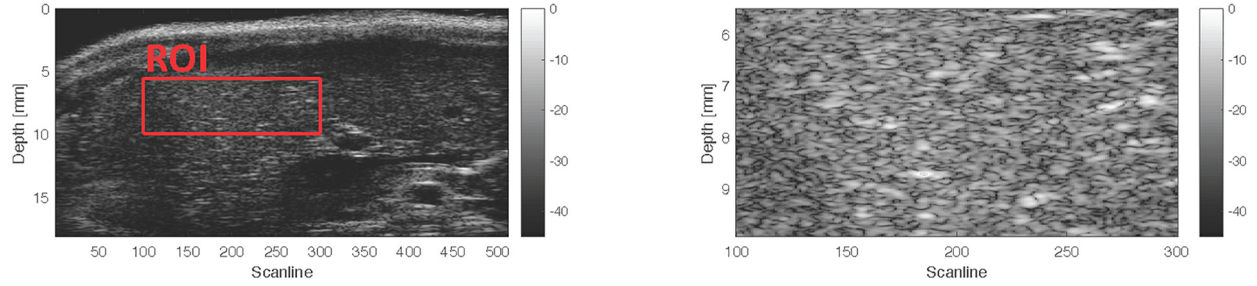
FIG. 6. (Color online) Left: ultrasound B-scan image from a 20 MHz scan of a normal rat liver, focused transmit at 11 mm depth. Right: zoom view of speckle region ROI selected for analysis.

Generally, in the range of interest ($2 < b < 4$), we find that the SNR is less than 1.5, which is below the theoretical 1.91 SNR found for fully-developed speckle under a Rayleigh PDF (Burckhardt, 1978; Tuthill *et al.*, 1988; Thijssen, 2003). However, it must be kept in mind that our underlying model of cylinders vs radius has a power law tail as the radius a goes to infinity, creating a long asymptotic tail of high echo amplitudes. In practice, each organ has a finite upper limit to the largest artery or vein, and this truncates the upper tail of the distribution, leading to a smaller standard deviation and a larger SNR than would be suggested by formulas.

III. METHODS

In the following examples, conventional B-scans were obtained using a Verasonics scanner with a 5 MHz ATL linear array transducer (V1, Verasonics, Inc., Kirkland, WA). A scan from a healthy adult was imaged under the requirements of informed consent and the University of Rochester Institutional Review Board. Rat experiments were reviewed and approved by the Institutional Animal Care and Use Committee of Pfizer, Inc., Groton, CT, where the ultrasound scan was acquired using a Vevo 2100 (VisualSonics, Toronto, CA) scanner and a 20 MHz center frequency transducer (data provided courtesy of Terri Swanson). Parameter estimation was performed using MATLAB (The Mathworks, Inc., Natick, MA) nonlinear least squares minimization of error, for two-parameter fits of the Burr distribution to the data.

IV. RESULTS

An ultrasound B-scan of a normal rat liver is shown in Fig. 6 (left), with a ROI denoted within the liver parenchyma where the pattern of echoes demonstrates a speckle pattern. This region is distal to the transmit focus, which is located at 11 mm depth. A close-up view is shown in Fig. 6 (right). The envelope of the beam-formed RF is distributed as shown in the histogram of Fig. 7, along with a theoretical Burr distribution with a power law parameter of $b = 3.4$, and an R^2 of 0.999. The match of this deterministic theory to the data is reasonable.

The normal human liver is shown in Fig. 8. This utilized five compounded plane wave transmit pulses with dynamic receive. The histogram of echo amplitudes is shown in Fig. 9 along with the Burr distribution fit with a power law parameter of $b = 2.9$ and an R^2 of 0.995.

To further examine the asymptotic characteristics of the histogram, we integrate the normalized histogram from the

rat liver data to form the CDF which is important in a number of statistical tests such as the Kolmogorov-Smirnov test (Feller, 1948). This is shown in Fig. 10 using the parameters found in Fig. 7 ($b = 3.4$ and $\lambda = 6.5 \times 10^5$) against the theoretical CDF for the Burr distribution, given by

$$\text{CDF}(A) = 1 - \left[1 + \left(\frac{A}{\lambda} \right)^2 \right]^{-(b-1)}. \tag{14}$$

The two functions (sampled histogram counts and theoretical function) are nearly indistinguishable on this scale and resolution.

Finally, because of the historic interest in the Rayleigh distribution (Burckhardt, 1978), the PDF for the rat liver is shown with the minimum mean squared error curve fit, shown in Fig. 11, where the Rayleigh PDF is given by

$$R(A) = \frac{A}{S^2} e^{\left(-A^2/2S^2 \right)}. \tag{15}$$

The overall shape of the Rayleigh distribution appears more compact and less suitable for the measured amplitude data.

V. DISCUSSION AND CONCLUSION

This framework postulates that the histogram of speckle amplitudes is determined by a simple Eq. (8) governed by
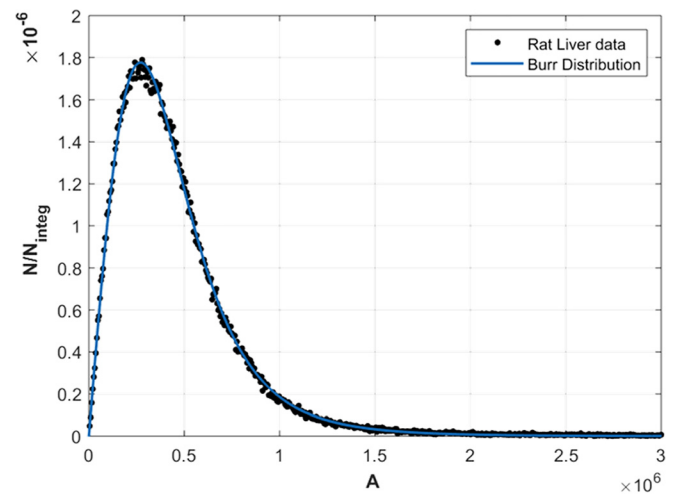

FIG. 7. (Color online) Histogram of echo amplitudes from the normal rat liver. Vertical axis = counts; horizontal axis = amplitudes of echo envelopes (arbitrary units). The dashed line indicates theoretical fit to the derived Eq. (10), with the power law parameter of $b = 3.4$ and $\lambda = 6.5 \times 10^5$.
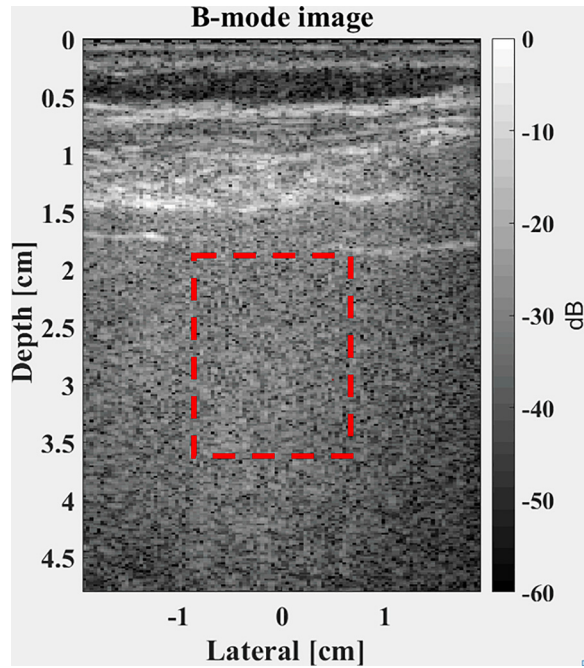
FIG. 8. (Color online) B-scan image of a healthy liver tissue in a human. A ROI is selected (dashed lines) for analysis.

four parameters: a power law b, a minimum cylinder size a_{min} above which the echo amplitude rises as a square root of radius, a vessel density N_0, and a scale amplitude A_0 depending on system factors such as amplifier gain. Furthermore, upon normalization of the histogram by its integral, the resulting PDF reverts to a Burr distribution first described in 1942 without any consideration of waves or scattering. The formulation is a major departure from the treatments over the last 100 yr in that the accounting is deterministic and focused on the maximum or predominant result in each step. Effectively, this means that each local maximum of the echoes is modeled as resulting from one dominant cylinder aligned perpendicular to the propagation direction of the pulse. Then, assuming a spatial ensemble

FIG. 10. (Color online) The comparison of the CDF of the rat liver echo amplitudes and the theoretical Burr distribution CDF.

large enough to encompass all radii according to the power law, the form of Eq. (8) is derived as the histogram of speckle envelopes within soft vascularized tissue. This formulation is limited by the major assumptions which simplify the derivations:

- The echoes are assumed to be produced by an isotropic ensemble of long cylindrical fluid-filled Born scatterers, dominated by those cylinders that are aligned perpendicular to the propagating pulse.
- The echoes from each generation of cylinders of radius a are mapped to an envelope amplitude of A by a square root function.
- The local maxima of envelopes dominate the histogram of sampled echoes.

Each of these assumptions are linked to a theoretical formula with examples; however, collectively they simplify the accounting of the overall chain of echo formation into a final histogram. Consequently, the issues of complex interference of phasors are not included in the analysis. In this sense our analysis returns to the earliest formulations of weak scattering from cylinders (Rayleigh, 1918b; Albini and Nagelberg, 1962).
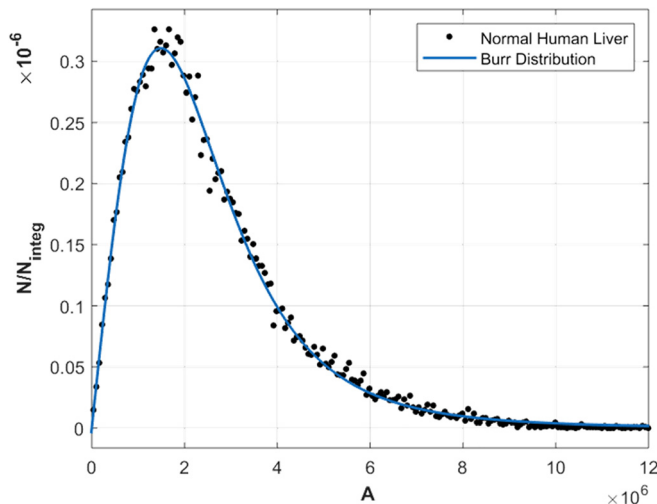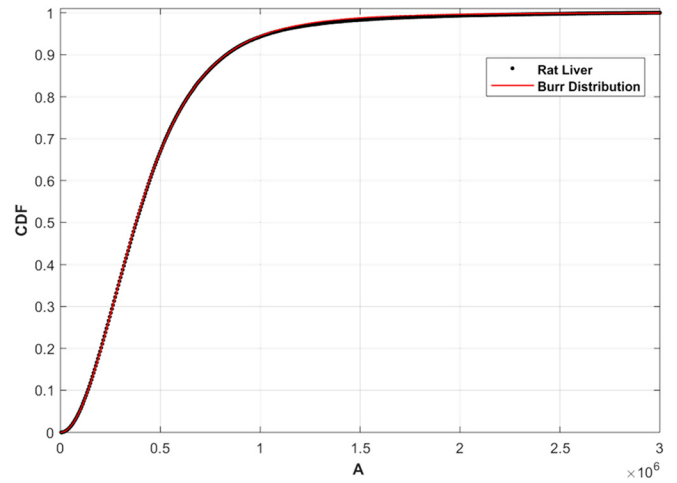

FIG. 9. (Color online) Data from a 5 MHz probe on a normal human liver with $b = 2.9$ and $\lambda = 3.3 \times 10^6$. Vertical axis: counts; horizontal axis: amplitudes of echo envelopes (arbitrary units).
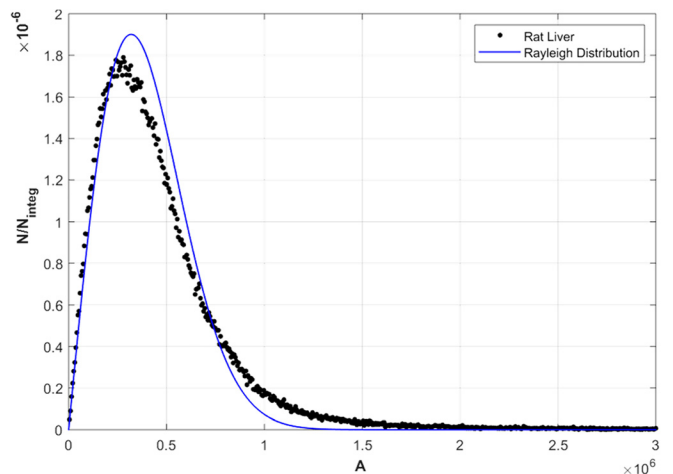

FIG. 11. (Color online) A comparison of the histogram of the rat liver echo amplitudes with a minimum mean squared error curve-fit to the classical Rayleigh distribution.

J. Acoust. Soc. Am. **146** (5), November 2019

Kevin J. Parker   3323

An important question which must be resolved by further studies of ensembles of human and animal soft tissue echoes is the following: will one of the theoretical distributions (Burr, Rayleigh, Rician, K, Homodyne-K, Gamma, or others) described in the literature be consistently the best fit, with lower mean squared errors, than all the others? A related question involves the sensitivity of the parameters to abnormalities that develop within the tissues and that change the scattering characteristics. Mathematically, we can say that the Burr distribution derived herein has an asymptotic behavior for high amplitudes that includes a power law proportional to A^{-2b}. In comparison, the other distributions derived in the classical literature have asymptotic behaviors related to Gaussian (Rayleigh), Gaussian times modified Bessel I_0 function (Rician), modified Bessel K functions (K distribution), or other transcendental functions (Gamma). The fractal branching vasculature hypothesis for scattering is naturally associated with a power law behavior describing the number of vessels of different diameter, and this power law b propagates through the derivations of the scattering functions and the final accounting of histogram amplitudes. Thus, a power law asymptotic behavior in amplitudes is plausible.

Finally, the important task of diagnosing abnormalities is left for further research. Presumably a disruption of the normal vascular structure in aggressive cancers would change the power law b and the vessel number density N_0, but the necessary clinical studies of these and other common pathologies are beyond the scope of this paper.

Further high resolution studies of the vasculature in 3D for different organs, along with corresponding high resolution B-scans of the same organs, would be helpful for testing and refining this theoretical framework of speckle amplitudes from soft vascularized tissues.

ACKNOWLEDGMENTS

FIG. 12. Schematic illustration following Papoulis showing the distribution of one continuous variable x with a distribution $f_x(x)$ which is mapped to a new distribution where $y = g(x)$, and retaining the area under the curve.

APPENDIX: MAPPING AND TRANSFORMATION OF FUNCTIONS

Herein we consider how the size distribution of cylindrical elements determines a distribution of echoes, in order to derive a histogram of echo amplitudes. A lucid explanation of the mapping of distributions is given in Chap. 5 of Papoulis (1987). This is explained in terms of PDFs, where a new variable is defined by $y = g(x)$, and x is a random variable with known PDF $f(x)$. However, the results hold for all well-behaved analytic functions where the area under the curve within any small interval is preserved by the mapping. We also assume a single valued mapping of $y = g(x)$ and its inverse $x = g^{-1}(y)$ for simplicity. In that case, by simply equating equal areas under some region of x_0 to $x_0 + \Delta x$, and mapping that to the y variable, the transformation rule is

$$f_y(y) = \frac{f_x(x)}{|dg(x)/dx|}, \tag{A1}$$

where on the right side the inverse function $x = g^{-1}(y)$ is then used to eliminate x as a variable and produce an equation in terms of y. The concept is illustrated in Fig. 12.

An important feature of this transformation for echo envelope functions emerges as a dramatic consequence, for anywhere near to a local maxima where the first derivative of the envelope approaches zero, the denominator term in Eq. (A1) approaches zero and the transformation produces a
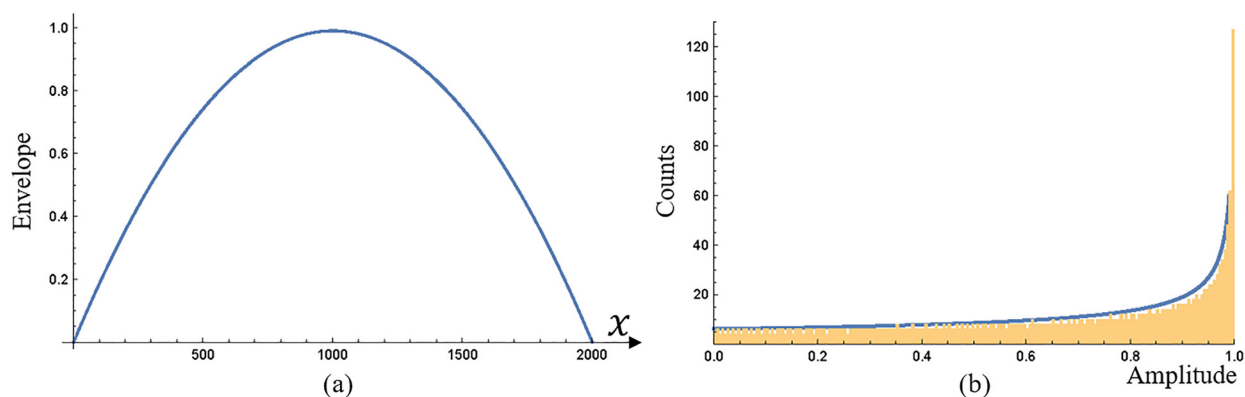

FIG. 13. (Color online) Example of sampling an envelope function (a) to produce a resulting histogram (b) and theory from Eq. (A1) (solid line). In (a), the vertical axis is amplitude, maximum value normalized to 1; the horizontal axis is time or distance, arbitrary units. In (b), the vertical axis is sampled counts in a histogram; the horizontal axis is echo amplitude. Note the spike near amplitude = 1, the local maximum of the envelope.
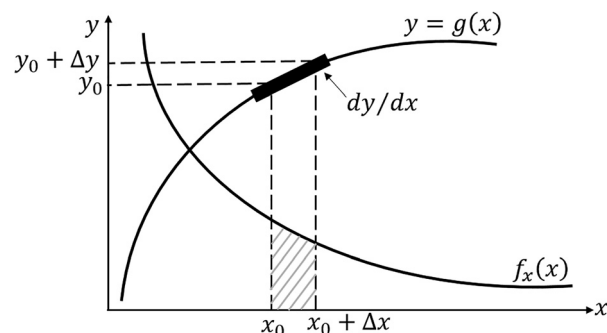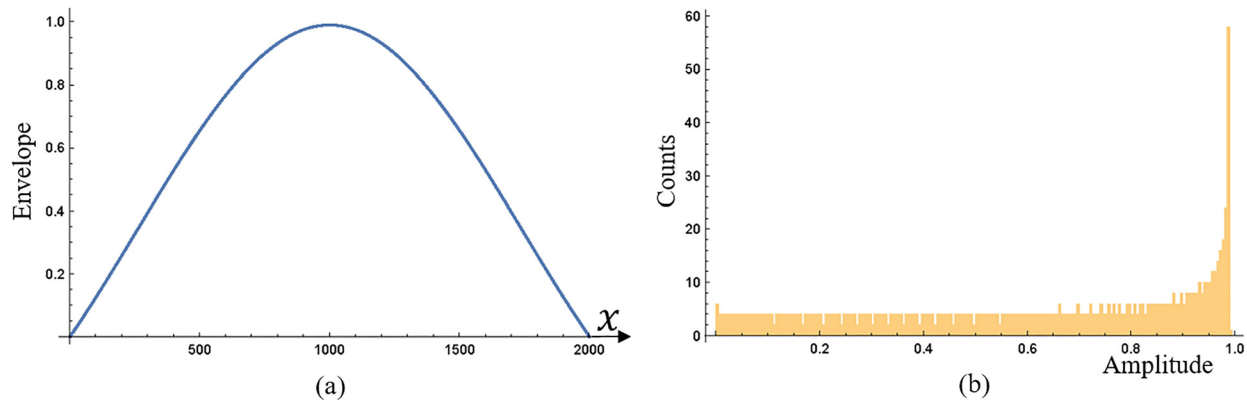
FIG. 14. (Color online) Second example using a modified Gaussian envelope in (a) and the resulting histogram in (b), demonstrating the dominant value or singularity mapped from the local maximum. In (a), the vertical axis is amplitude, maximum value normalized to 1; the horizontal axis is time or distance, arbitrary units. In (b), the vertical axis is sampled counts in a histogram; the horizontal axis is echo amplitude. Note the spike near amplitude = 1, the local maximum of the envelope.

singularity around that point. Thus, as we apply this to echo envelopes where x is the echo space or time variable and y is the echo envelope, each local maximum creates a large spike in the histogram of the envelope.

As an example, let $y = A_1(1 - x^2)$ for $-1 < x < 1$. By symmetry, we only need to consider $0 < x < 1$ and assume uniform likelihood of sampling within this interval so $f_x(x) = 1$. Also, $|dy/dx| = A_1 \cdot 2x$ and $x = g^{-1}(y) = \sqrt{1 - (y/A_1)}$. Finally, from Eq. (A1), $f(y) = 1/[2A_1\sqrt{1 - (y/A_1)}]$ for $0 < y < A_1$, which has a singularity as $y \rightarrow 1$ [the value of the local maximum of $y = f(x)$]. This is illustrated in Fig. 13 for $A_1 = 1$.

Another example of a modified Gaussian is shown in Fig. 14, where $y = \mathbf{e}^{-x^2/2}(1 - x^2)$, producing a similar result deriving from the singularity produced by the local maximum of the envelope function.

Thus, we conclude that the histogram of envelopes contains a dominant contribution formed by the local maximum, where the first derivative approaches zero. This dominant contribution from the local maximum of the echo is also assumed to be proportional to the RMS echo amplitude formed by convolution, Eq. (6), and then is used in the superposition or summation over all cylinder sizes in our formulation.

Abramowitz, M., and Stegun, I. A. (**1964**). *Handbook of Mathematical Functions with Formulas, Graphs, and Mathematical Tables* (U.S. Government Printing Office, Washington, DC).

Albini, F. A., and Nagelberg, E. R. (**1962**). "Scattering of a plane wave by an infinite inhomogeneous, dielectric cylinder—an application of the Born approximation," J. Appl. Phys. **33**, 1706–1713.

Bamber, J. C., and Dickinson, R. J. (**1980**). "Ultrasonic B-scanning: A computer simulation," Phys. Med. Biol. **25**, 463–479.

Bracewell, R. N. (**1965a**). *The Fourier Transform and its Applications* (McGraw-Hill, New York), Chap. 8.

Bracewell, R. N. (**1965b**). *The Fourier Transform and its Applications* (McGraw-Hill, New York), Chap. 12.

Burckhardt, C. B. (**1978**). "Speckle in ultrasound B-mode scans," IEEE Trans. Sonics Ultrason. **25**, 1–6.

Burr, I. W. (**1942**). "Cumulative frequency functions," Ann. Math. Stat. **13**, 215–232.

Campbell, J. A., and Waag, R. C. (**1984a**). "Measurements of calf liver ultrasonic differential and total scattering cross sections," J. Acoust. Soc. Am. **75**, 603–611.

Campbell, J. A., and Waag, R. C. (**1984b**). "Ultrasonic scattering properties of three random media with implications for tissue characterization," J. Acoust. Soc. Am. **75**, 1879–1886.

Chivers, R. C. (**1977**). "The scattering of ultrasound by human tissues-some theoretical models," Ultrasound Med. Biol. **3**, 1–13.

Cramblitt, R. M., and Parker, K. J. (**1999**). "Generation of non-Rayleigh speckle distributions using marked regularity models," IEEE Trans. Ultrason. Ferroelectr. Freq. Control **46**, 867–874.

Feller, W. (**1948**). "On the Kolmogorov-Smirnov limit theorems for empirical distributions," Ann. Math. Statist. **19**, 177–189.

Fontaine, I., Savery, D., and Cloutier, G. (**2002**). "Simulation of ultrasound backscattering by red cell aggregates: Effect of shear rate and anisotropy," Biophys. J. **82**, 1696–1710.

Gore, J. C., and Leeman, S. (**1977**). "Ultrasonic backscattering from human tissue: A realistic model," Phys. Med. Biol. **22**, 317–326.

Insana, M. F., and Brown, D. G. (**1993**). "Acoustic scattering theory applied to soft biological tissues," in *Ultrasonic Scattering in Biological Tissues*, edited by K. K. Shung and G. A. Thieme (CRC Press, Boca Raton, FL), pp. 75–124.

Insana, M. F., Wagner, R. F., Brown, D. G., and Hall, T. J. (**1990**). "Describing small-scale structure in random media using pulse-echo ultrasound," J. Acoust. Soc. Am. **87**, 179–192.

Kutay, M. A., Petropulu, A. P., and Piccoli, C. W. (**2001**). "On modeling biomedical ultrasound RF echoes using a power-law shot-noise model," IEEE Trans. Ultrason. Ferroelectr. Freq. Control **48**, 953–968.

Kutay, M. A., Petropulu, A. P., and Piccoli, C. W. (**2003**). "Breast tissue characterization based on modeling of ultrasonic echoes using the power-law shot noise model," Pattern Recogn. Lett. **24**, 741–756.

Landini, L., and Verrazzani, L. (**1990**). "Spectral characterization of tissues microstructure by ultrasounds: A stochastic approach," IEEE Trans. Ultrason. Ferroelectr. Freq. Control **37**, 448–456.

Laporte, C., Clark, J. J., and Arbel, T. (**2009**). "Generalized Poisson 3-D scatterer distributions," IEEE Trans. Ultrason. Ferroelectr. Freq. Control **56**, 410–414.

Lizzi, F. L., Greenebaum, M., Feleppa, E. J., Elbaum, M., and Coleman, D. J. (**1983**). "Theoretical framework for spectrum analysis in ultrasonic tissue characterization," J. Acoust. Soc. Am. **73**, 1366–1373.

Macovski, A. (**1983**). *Basic Ultrasonic Imaging* (Prentice-Hall, Englewood Cliffs, NJ).

Mamou, J., and Oelze, M. L. (**2013**). *Quantitative Ultrasound in Soft Tissues* (Springer Netherlands, Dordrecht).

Morse, P. M., and Ingard, K. U. (**1987**). *Theoretical Acoustics* (Princeton University Press, Princeton, NJ), Chap. 8.

Papoulis, A. (**1987**). *The Fourier Integral and its Applications* (McGraw-Hill, New York).

Parker, K. J. (**2016**). "The H-scan format for classification of ultrasound scattering," J. OMICS Radiol. **5**, 1000236.

Parker, K. J. (**2019**). "Shapes and distributions of soft tissue scatterers," Phys. Med. Biol. **64**(17), 175022.

Parker, K. J., Carroll-Nellenback, J. J., and Wood, R. W. (**2019**). "The 3D spatial autocorrelation of the branching fractal vasculature," Acoust. **1**, 369–381.

J. Acoust. Soc. Am. **146** (5), November 2019

Kevin J. Parker   3325

Poularikas, A. D. (**2010**). "Transforms and applications handbook, Chapter 6," in *The Electrical Engineering Handbook Series* (CRC Press, Boca Raton, FL), p. 7.21.

Prince, J. L., and Links, J. M. (**2015**). *Medical Imaging Signals and Systems* (Pearson, Boston, MA).

Rayleigh, L. (**1897**). "XXXVII. On the passage of waves through apertures in plane screens, and allied problems," Philos. Mag. **43**, 259–272.

Rayleigh, L. (**1918a**). "On the scattering of light spherical shells, and by complete spheres of periodic structure, when the refractivity is small," Proc. Royal Soc. London Series A **94**, 296–300.

Rayleigh, L. (**1918b**). "XLI. The dispersal of light by a dielectric cylinder," London, Edinburgh, Dublin Philos. Mag. J. Sci. **36**, 365–376.

Rodriguez, R. N. (**1977**). "A guide to the Burr type XII distributions," Biometrika **64**, 129–134.

Savery, D., and Cloutier, G. (**2001**). "A point process approach to assess the frequency dependence of ultrasound backscattering by aggregating red blood cells," J. Acoust. Soc. Am. **110**, 3252–3262.

Savery, D., and Cloutier, G. (**2005**). "Effect of red cell clustering and anisotropy on ultrasound blood backscatter: A Monte Carlo study," IEEE Trans. Ultrason. Ferroelectr. Freq. Control **52**, 94–103.

Shung, K. K., and Thieme, G. A. (**1993**). *Ultrasonic Scattering in Biological Tissues* (CRC Press, Boca Raton, FL).

Sleefe, G. E., and Lele, P. P. (**1988**). "Tissue characterization based on scatterer number density estimation," IEEE Trans. Ultrason. Ferroelectr. Freq. Control **35**, 749–757.

Thijssen, J. M. (**2003**). "Ultrasonic speckle formation, analysis and processing applied to tissue characterization," Pattern Recogn. Lett. **24**, 659–675.

Tuthill, T. A., Sperry, R. H., and Parker, K. J. (**1988**). "Deviations from Rayleigh statistics in ultrasonic speckle," Ultrason. Imag. **10**, 81–89.

Waag, R. C., Dalecki, D., and Christopher, P. E. (**1989a**). "Spectral power determinations of compressibility and density variations in model media and calf liver using ultrasound," J. Acoust. Soc. Am. **85**, 423–431.

Waag, R. C., Dalecki, D., and Smith, W. A. (**1989b**). "Estimates of wave front distortion from measurements of scattering by model random media and calf liver," J. Acoust. Soc. Am. **85**, 406–415.

Waag, R. C., Lee, P. P. K., Persson, H. W., Schenk, E. A., and Gramiak, R. (**1982**). "Frequency-dependent angle scattering of ultrasound by liver," J. Acoust. Soc. Am. **72**, 343–352.

Wear, K. A., Wagner, R. F., Brown, D. G., and Insana, M. F. (**1997**). "Statistical properties of estimates of signal-to-noise ratio and number of scatterers per resolution cell," J. Acoust. Soc. Am. **102**, 635–641.

Zagzebski, J. A., Lu, Z. F., and Yao, L. X. (**1993**). "Quantitative ultrasound imaging: In vivo results in normal liver," Ultrason. Imag. **15**, 335–351.